




On the morphology of grain boundary discontinuous reactions and phase identification in an advanced Cr–Fe–Ni alloy

J. C. Spadotto^{1,2,*} , M. G. Burke², and I. G. Solórzano¹

¹Department of Chemical and Materials Engineering, PUC-Rio, Rio de Janeiro 22451-900, Brazil

²Materials Performance Centre, School of Materials, The University of Manchester, Oxford Road, Manchester M13 9PL, UK

Received: 17 January 2020

Accepted: 15 April 2020

Published online:

26 April 2020

© Springer Science+Business Media, LLC, part of Springer Nature 2020

ABSTRACT

Grain boundary (GB) precipitation phenomena in Alloy 33 that occurred during isothermally aging at 800 °C for periods of 1–10 h have been studied by scanning electron microscopy, and analytical electron microscopy (including scanning/transmission electron microscopy (STEM/TEM), X-ray energy-dispersive spectroscopy (XEDS), and electron diffraction). The type and morphology of phases formed during discontinuous precipitation (DP) resulting from the combined effect of GB migration, diffusion, and precipitation processes have been investigated. STEM-XEDS maps and electron diffraction data have shown that the DP reaction products resulted in the precipitation of 3 different phases within the same colony: (1) face-centred cubic Cr-rich $M_{23}C_6$, (2) diamond-cubic Si-enriched M_6N , and (3) lamellar body-centred cubic α -Cr phase. In general, DP colonies in this alloy system develop as follows: at early stages of the aging process intergranular precipitation of $M_{23}C_6$ and M_6N occurs at original GB; with increasing aging time, some GBs migrate with the concomitant precipitation of lamellar α -Cr-rich phase, thereby developing DP colonies. The necessary solute partitioning is operated by interface diffusion mechanism through the GB acting as reaction front. Besides the occurrence of three different precipitated phases within the same DP colony, the most remarkable characteristic in the overall the precipitation process in this alloy system refers to consistent evidence that the original intergranular precipitates are different from the lamellar phase that precipitates in association with the migrating GB. This study provides the first report of this observation in a complex multiphase discontinuous GB precipitation reaction and evidence for DP phenomena involving three different precipitated phases.

Address correspondence to E-mail: juliocspadotto@gmail.com

Introduction

Grain boundary (GB) phenomena, including discontinuous precipitation and diffusion-induced GB migration (DIGM), are of increasing interest. From the fundamental point of view, these phenomena are particularly intriguing because of the synergy among GB migration, solute redistribution, and precipitation processes. From the practical perspective, it is important to understand these phenomena in order to prevent undesirable effects on the mechanical and corrosion performance of structural alloys. Such effects are widely reported to occur in several types of alloys used in high-performance industries [1–11]. One of the most interesting GB reactions observed in structural alloy systems is the discontinuous precipitation (DP) reaction. This phenomenon involves concurrent precipitation accompanying GB migration, for which DIGM may act as precursor for DP and provide the driving force for boundary migration [12, 13].

The DP reaction is a diffusion-controlled phenomenon driven by a migrating GB, which acts as a fast diffusion path under the action of chemical and capillary forces; the migrating GB leaves behind a regularly spaced array of lamellar or rod-like equilibrium precipitates that have nucleated and grown cooperatively from the supersaturated matrix [14, 15]. This phenomenon has been documented to occur in over one hundred binary systems and in several ternaries and multicomponent alloys [5, 16, 17]. The occurrence of DP is highly dependent on the energy, mobility, and diffusivity of the boundary, which, in turn, depends on the structural characteristics of the individual GB [18].

The growth characteristics of DP in binary alloys containing only substitutional solute atoms are different from those observed in multicomponent alloy systems containing both substitutional and interstitial solutes. In the former, the transport of solute is through the migrating GB reaction front, allowing the composition of the matrix ahead the reaction front and the rate of the GB migration to be constant, i.e. a steady-state reaction [5, 15, 17]. On the other hand, in multicomponent alloys containing both substitutional and interstitial atoms, a key factor controlling the solute redistribution is the difference in the diffusion mechanism (substitutional versus interstitial diffusion), which results in a non-steady-state reaction and

makes these systems more complex for the study of the DP phenomenon [7, 19].

DP reactions have been reported to occur in several structural multicomponent materials, such as austenitic stainless steel [2, 6–8, 20–27], Ni-based alloys [28–31], Ni–Fe–Cr alloys [4, 32, 33], and duplex and super-duplex stainless steels [3, 34]. In such multicomponent alloy systems containing both substitutional and interstitial solutes, the DP colonies consist of either Cr-rich $M_{23}C_6$ [3, 4, 20, 21, 25, 28–33, 35] or Cr-rich M_2N -nitrides [2, 6–8, 19, 22–24, 26, 27, 34] with a lamellar morphology (where M can be Cr, Ni, Fe, Mo, and Si). However, DP colonies in high Mo-containing austenitic stainless steel have been reported to contain lamellar σ -phase rather than Cr-rich M_2N -nitrides or Cr-rich $M_{23}C_6$ -carbides [36]. In addition to the discontinuous lamellar σ -phase, the precipitation of both chromium nitride (Cr_2N) and hexagonal intermetallic R-phase has been reported to occur within the colony with increasing aging time [36]. Moreover, an unusual form of DP colonies has also been reported in Ni-based alloys, in which a biphasic-supersaturated matrix (matrix + precipitates) decomposes into a DP colony containing three different phases [37–39].

The present investigation deals with GB precipitation phenomena in Alloy 33, an advanced high Cr–Fe–Ni alloy with high strength and excellent corrosion resistance [40, 41]. In fact, in recent years, this alloy has become a potential candidate for accident tolerant applications in nuclear energy systems at high temperatures [42, 43]. In previous studies [44, 45], it had been reported that isothermally aged Alloy 33 developed DP colonies characterized by the presence of multiple precipitated phases. Cr-rich lamellar precipitates, in addition to a Si-enriched phase, were observed within the DP colonies, but these phases were not identified. This paper, therefore, is focused on the detailed characterization and identification of the various phases formed within the DP colony in Alloy 33 upon thermal aging and aims to provide an improved understanding of the precipitation sequence and resulting microstructure. For this purpose, analytical transmission electron microscopy (ATEM) and electron diffraction analyses have been used extensively. Based on detailed microstructure observations, new insights into the mechanisms and evolution of the discontinuous reaction products in complex systems are also discussed.

Experimental procedure

The material used in this study is a commercial corrosion-resistance alloy based on Cr-Fe-Ni-N named Nicrofer 3033, or Alloy 33. The as-received material was a solution-treated 5-mm-thick rolled plate with a chemical composition shown in Table 1.

Samples in the as-received condition were isothermally aged at 800 °C for 1 h, 2 h, 5 h, and 10 h. All specimens were water-quenched after aging. In order to observe and document the effect of aging on the microstructure at the micro- and nano-scales, the samples were analysed by light optical microscopy (LOM—Axioplan 2—Carl Zeiss), scanning electron microscopy (SEM), and scanning/transmission electron microscopy (STEM/TEM) with X-ray energy-dispersive spectroscopy (XEDS). All samples for LOM, SEM, and STEM/TEM analyses were prepared following the same procedure. Discs (3 mm in diameter and approximately 100 µm thick) were extracted from the mechanically thinned aged samples. Thin foils were then produced by twin-jet electrolytic polishing (TenuPol 5—Struers) using a solution of 20% HClO₄ and 80% CH₃OH at ~ -35 to -40 °C and 14 V. Detailed microstructural observation of the samples was performed using field emission gun scanning electron microscopy (FEGSEM) (JEOL JSM 7100F, FEI Magellan 400 XHR and Zeiss Sigma VP FEG) at 5 kV. The Zeiss Sigma was equipped with a Si drift detector (SDD) for XED spectrometry (Oxford Instruments X-Max 150 SDD) and Aztec analysis system. FEGSEM-XED spectrum imaging (SI) datasets were acquired at 15 kV with a pixel dwell time of 300 µs and a total acquisition time of 900 s for SEM-XED SI datasets.

TEM characterization was performed on electron-transparent specimens using a variety of microscopes, including a Phillips CM20 200 kV (LaB₆), FEI Tecnai G2 200 kV (LaB₆), JEOL FEG JEM 2100F 200 kV, FEI Tecnai TF30 FEG 300 kV. Imaging and chemical composition analyses of the precipitates were performed in STEM mode using an FEI TALOS F200A with an X-FEG and SuperX (4 SDDs) XED analysis system. In this study, the discrete STEM-XEDS spot analyses were performed with the

acquisition live time of 100 s for each spectrum and STEM-XED spectrum image (SI) datasets were acquired with a dwell time of 500 µs per pixel and a total acquisition time of 1800 s. All Talos STEM-XEDS data were processed using FEI Velox 2.3 software with theoretical k-factors. All elemental maps extracted from the XED SI datasets were background-subtracted, deconvoluted, and processed using the appropriate software. It is noted that no composition values are presented with these maps due to the semi-quantitative nature of these analyses.

Discrete STEM/XEDS spot analyses for semi-quantitative analyses were performed using the FEI Tecnai G2 LaB₆ analytical TEM/STEM operated at 200 kV and equipped with an Oxford Instrument X-Max 80 TLE SDD and Aztec analysis system.

Results and discussion

LOM and SEM characterization of aged alloy 33 microstructure

As reported in previous work [44], the microstructure in the as-received condition sample consisted of equiaxed recrystallized FCC grains. Figure 1 presents a series of LOM images showing the microstructure evolution of the Alloy 33 as a function of aging at 800 °C for periods from 1 h up to 10 h. As shown in Fig. 1a, after 1 h of aging, intergranular precipitates (indicated by the arrows) have formed along nearly all GBs. These images were obtained from bulk regions of the electropolished TEM specimens; thus, these “bulk” (thick) regions were characterized by a light electroetch. In Fig. 1b, the extent of intergranular precipitation appears to have increased after 2 h at 800 °C, but some boundaries are precipitate-free. After 5 h at 800 °C (Fig. 1c), the extent of intergranular and intragranular precipitation has increased, and “puckers” in addition to a well-developed DP colony (indicated by the arrow) can be observed. The 10 h aging treatment promoted the formation of larger, well-developed DP colonies as well as significant intragranular precipitation.

Table 1 Chemical composition of Alloy 33 (wt%)

Cr	Fe	Ni	Mo	Cu	N	C	Mn	P	S	Si
32.75	32.54	31.35	1.49	0.54	0.40	0.012	0.63	0.014	0.002	0.30

Figure 1 LOM images obtained from lightly electroetched samples of Alloy 33 aged at 800 °C for **a** 1 h; **b** 2 h; **c** 5 h; and **d** 10 h.

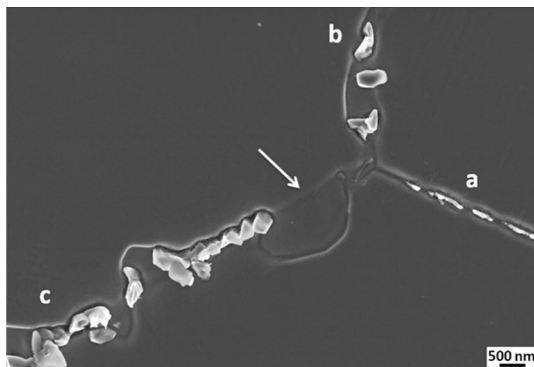
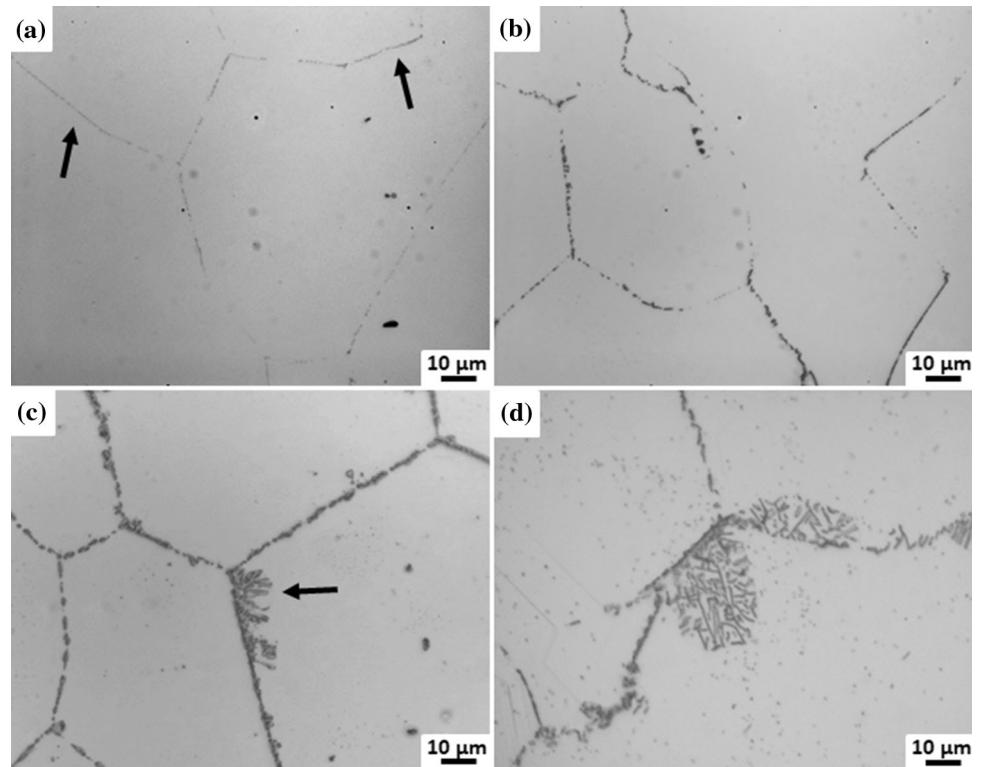


Figure 2 Secondary electron (SE) image of a triple point region in Alloy 33 aged at 800 °C for 1 h. The original position of GB “c” is arrowed.

Figure 2 shows a secondary electron (SE)-SEM image of a triple point in Alloy 33 aged at 800 °C for 1 h showing three GBs with coarse precipitates of various sizes and morphologies. Whereas the GB located at the right side of this figure, labelled “a”, has remained static, the GB identified as “b” has migrated in one direction with concomitant precipitation, and the GB labelled “c” shows evidence of migration in both directions and shows both coarse precipitation and precipitate-free regions in a manner suggesting the occurrence of DIGM. At this stage, DP

colony has not been developed, so one can argue that GB migration precedes DP or occurs at the early stages of the DP reaction in Alloy 33.

Figure 3 provides two examples of different DP colonies observed in Alloy 33 after aging at 800 °C for 2 h. In both examples, precipitates decorating the original GB position were observed in addition to GB migration into the FCC matrix of the adjacent grain. The growth of some precipitates along the migrated boundary is clearly evident. The specific DP colony shown in Fig. 3b provides an example of branched lamellar precipitates, indicated by the arrows, associated with the migrating GB. This mechanism of lamellae multiplication has long been reported in binary systems [46].

Figure 4a displays a low-magnification SE image of Alloy 33 aged at 800 °C for 5 h showing precipitation products occurring at all GBs, as well as DP colonies, indicated by the arrows. Some DP colonies observed in this aged material exhibited distinct differences in the size and morphology of the precipitates. Figure 4b, which is obtained from the region indicated by the red box in Fig. 4a, shows the difference in extent of intergranular precipitation at three different GBs after aging at 800 °C for 5 h. In this figure, the DP colony appears to be comprised of lamellar

Figure 3 SE images of DP colonies observed in Alloy 33 aged at 800 °C for 2 h.

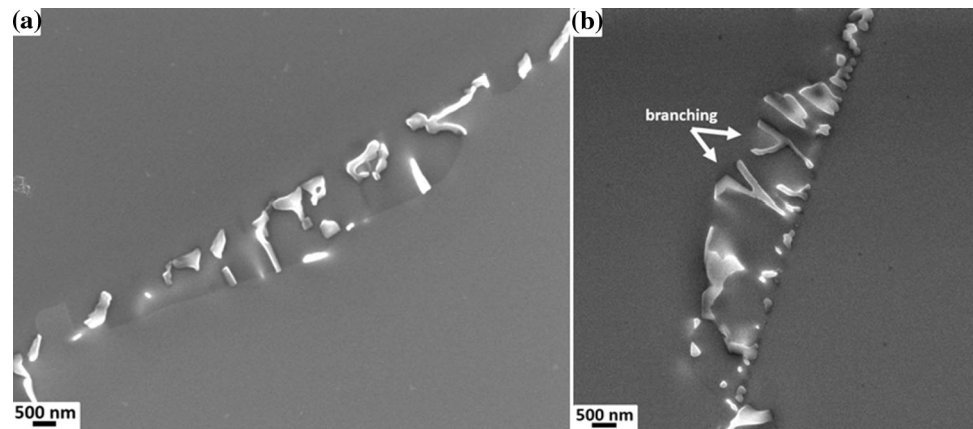
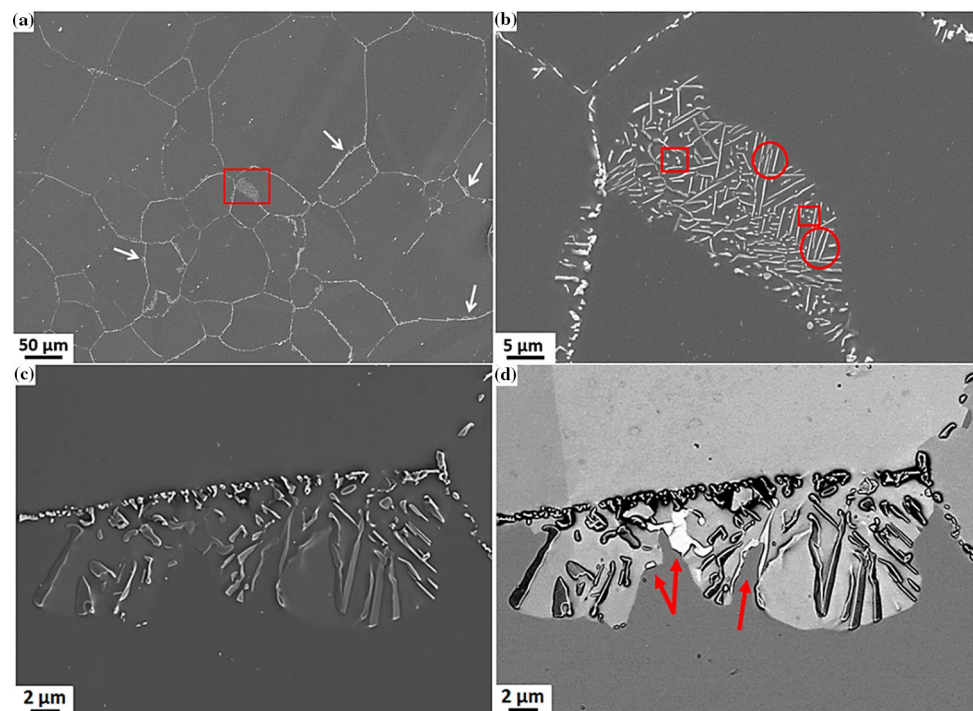


Figure 4 **a** Low-magnification SE image of Alloy 33 aged at 800 °C for 5 h; **b** SE image showing a well-developed DP colony marked by the red box in **a**; **c** SE; and **d** complementary backscattered electron (BSE) images of a DP colony showing different precipitate morphologies present in the aged alloy.



precipitates with different crystallographic orientations. Although both lamellar and discrete precipitates appear to have nucleated at original GB position, a complex distribution of precipitates can be observed within the “colony”: both lamellar (indicated by the circles) and nodular precipitate morphologies (indicated by the squares) are visible. Multiple “variants” of the lamellar DP precipitates are evident—each “variant” has grown in a different crystallographic direction. This finding corroborates the observation of lamellar and “nodular” (discrete) precipitates within the DP colonies reported by several authors [7, 8, 18, 26, 31, 35, 37, 39]. However, careful examination of the “colony” suggests that it

may be the result of multiple intersecting DP colonies, which would not be unexpected given the location of this colony near multiple GBs. Complementary SE/BSE-SEM images in Fig. 4c and 4d show a typical single DP colony in which discrete precipitates decorated the original GB position, whereas lamellar precipitates formed behind the migrating GB as it moved into the adjacent FCC grain. Such observation has been consistent throughout this investigation. As a rule of DP reaction, the orientation of the initial grain is extended with the colony, resulting in that the region swept by the boundary migrating has the same orientation as the matrix from which the lamella starts to grow. This is evident in

the BSE image of Fig. 4d in which the parent grain and solute-depleted matrix in the migrated area exhibit the same electron channelling (orientation) contrast. Furthermore, three different phases have been identified in the DP colony: the FCC matrix, lamellar and small discrete precipitates (grey features), and brightly imaging phases (high Z-contrast) at DP reaction front as indicated by the red arrows.

Aging for 10 h at 800 °C promoted extensive intergranular and intragranular precipitation, as shown in Fig. 5a. The fine intragranular precipitates exhibited a needle-like morphology. Such homogeneous precipitates do not appear prominently in this low-magnification SE image; however, higher magnification images are shown in the inset in this figure. It is worth highlighting that the lamellar DP precipitates, which have grown parallel to each other, had nucleated adjacent to GB, and not at the GB (as stated by the classical theory of discontinuous precipitation). The elemental maps extracted from the SEM-EDX SI datasets in Fig. 5b show the partitioning of Cr, Fe, Ni, Si, and Mo in those two regions identified in Fig. 5a. All precipitates were Cr-rich, some were also enriched in Si, but the lamellar precipitates were Si-free. It was noted that the Si-enriched phase precipitated primarily at original GB position.

Based on morphological and analytical observations of Alloy 33 in samples aged at 800 °C, it can be stated that the DP colonies develop with the following characteristics: (1) Cr-rich precipitates nucleated at GBs in the early stages of aging and continue to grow with time at temperature; (2) Si-enriched phase precipitated at the original GB position and grew adjacent to the intergranular Cr-rich precipitates; (3) as the aging time increased, Cr-rich phases nucleated adjacent to GB and grew as lamellar precipitates behind the migrating GB; (4) eventually, Si-enriched precipitates formed within the DP colony behind the migrated grain boundary.

ATEM characterization and phase identification

In this section, the analyses of the various phases formed during isothermal aging at 800 °C for 1 up to 10 h using ATEM and selected area electron diffraction (SAED) are presented. The BF-STEM image in Fig. 6 shows a GB that had locally migrated during precipitation at this boundary after aging for 1 h. The precipitate morphology has accommodated the

“bulging” boundary and has grown along the migrated boundary. Figure 6 also shows the corresponding STEM-XEDS maps of main elements associated with precipitation during aging for 1 h. These precipitates, which were the first to nucleate in Alloy 33 at 800 °C, were identified by SAED as FCC $M_{23}C_6$. The [101] SAED pattern shown in Fig. 6 also confirmed the well-known cube-on-cube orientation relationship (O.R.) between the $M_{23}C_6$ and the FCC matrix: $[101]_{M_{23}C_6} // [101]_{FCC\ matrix}$. Both lattices share a cubic symmetry and differ in lattice parameter by a factor of ~ 3 . STEM-XEDS maps confirmed that the GB precipitates were enriched in Cr and Mo. Concomitant with the precipitation of the Cr-enriched carbides, Cr-depleted, and Fe–Ni-enriched zones were observed in the regions behind the migrated boundary.

Cr-rich $M_{23}C_6$ has a FCC structure (space group: $Fm\bar{3}m$) and lattice parameter of $a = 1.050\text{--}1.070$ nm [21, 25, 31, 47–50], which is approximately 3 times larger than of the FCC matrix, as shown in Fig. 6. The variation in lattice parameter of this carbide has been associated with the increase in Mo content [47, 51]. Several authors [21, 25, 31, 35, 47, 48] have reported the $M_{23}C_6$ /FCC matrix O.R. being cube-on-cube: $(100)_{M_{23}C_6} // (100)_{FCC\ matrix}$ and $[100]_{M_{23}C_6} // [100]_{FCC\ matrix}$, which is the same O.R. found in this investigation. This carbide has been reported in the literature to be rich in Cr, containing Mo, Fe, and Ni. Although compositionally very stable and usually reported to be Si-free [47, 49, 50, 52], some authors have found $M_{23}C_6$ containing Si [53].

In order to determine the solute partitioning associated with the precipitates and the early stages of the DP reactions at the GB, STEM-XEDS experiments were performed. Figure 7 shows a BF-STEM image of a specific GB in Alloy 33 aged at 800 °C for 1 h and the corresponding XEDS maps. Discrete precipitates are evident along a “wavy” grain boundary. This figure confirms the same qualitative composition of the precipitates shown in Fig. 6: all precipitates were Cr-rich with some Mo, identified as $M_{23}C_6$ with FCC structure. Also in Fig. 7, a Si-enriched feature, which is indicated by the yellow arrow, was detected adjacent to an $M_{23}C_6$, and qualitative evidence of Cr-depletion associated with the precipitation of $M_{23}C_6$ can be observed.

Figure 8 contains a set of diffraction contrast TEM images intended to illustrate characteristics of the

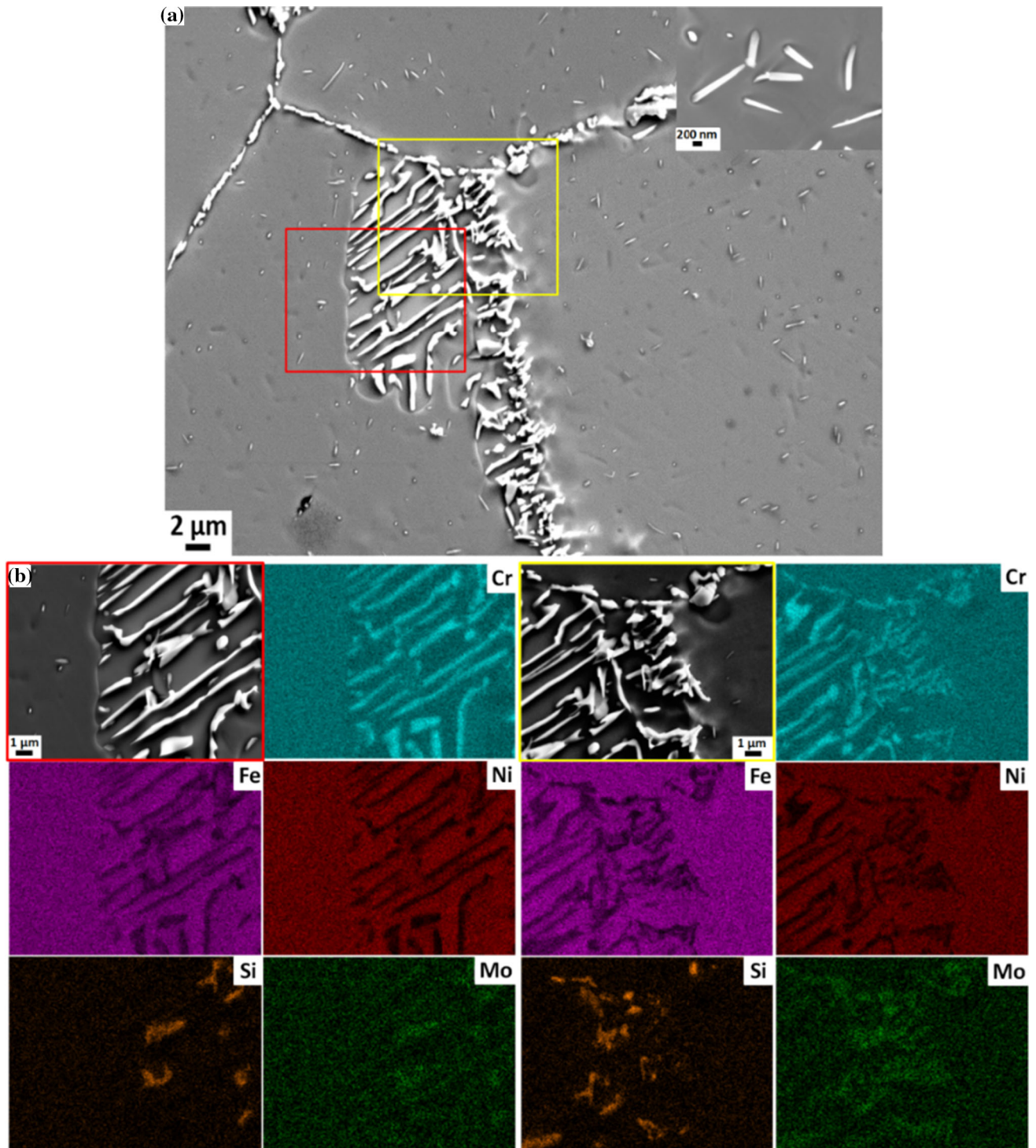


Figure 5 **a** SE image of Alloy 33 aged at 10 h showing a well-developed DP colony and **b** corresponding XEDS maps of Cr, Fe, Ni, Si, and Mo obtained from the regions indicated in **a**.

discontinuous reaction in Alloy 33, which includes grain boundary migration and precipitation processes associated with aging at 800 °C for 1 h. The BF-TEM image in Fig. 8a shows a pronounced

boundary curvature of the upper strongly diffracting grain. The centred dark-field (CDF)-TEM image in Fig. 8b with a grain reflection contrast illustrates the extent of the GB bowing and migration. Notice in this

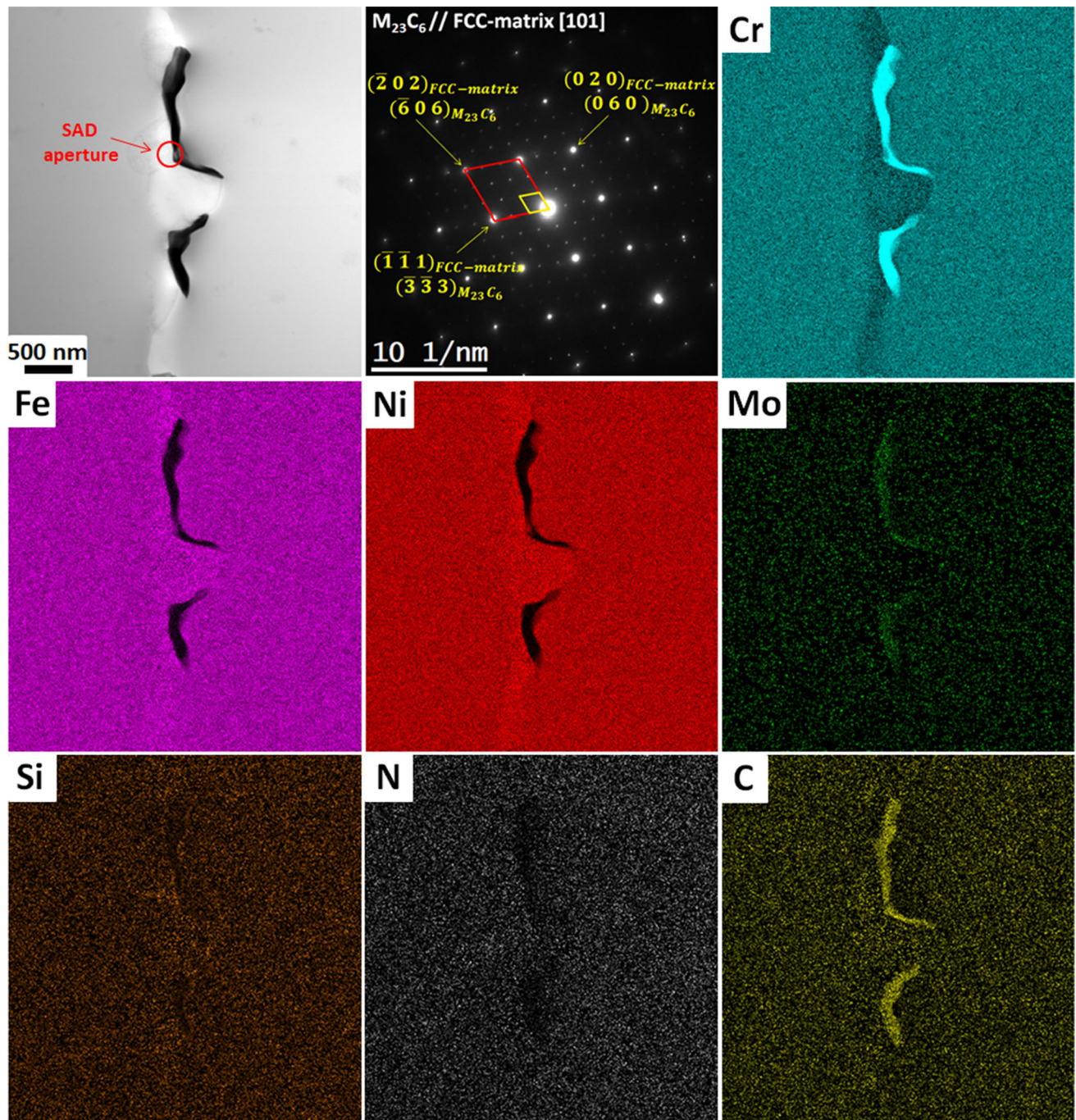


Figure 6 BF-STEM image of intergranular Cr-rich $M_{23}C_6$ and the locally migrated grain boundary resulting from aging at 800 °C for 1 h; SAED pattern obtained from the region indicated by the circle, $z = [101]_{M_{23}C_6} \parallel [101]_{FCC\ matrix}$; and corresponding XEDS

image that some carbides are located at the original GB position. The complex morphology of the $M_{23}C_6$ formed during aging at 800 °C is shown in Fig. 8c, in which carbides nucleated at the original GB position

maps of Cr, Fe, Ni, Mo, Si, N, and C extracted from STEM-XEDS dataset.

grew along the migrating boundary (indicated by the red arrows).

In addition to Cr-rich $M_{23}C_6$ at original GB position in Fig. 8, the existence of another type of precipitated phase has been verified, which is indicated by the

Figure 7 BF-STEM image of GB precipitates a “wavy” boundary in Alloy 33 aged at 800 °C for 1 h and corresponding XEDS maps of Cr, Fe, Ni, Mo, Si, C, and N extracted from the STEM-XED SI dataset. The arrows point the Si-enriched zone adjacent to both Cr-depleted zone and $M_{23}C_6$.

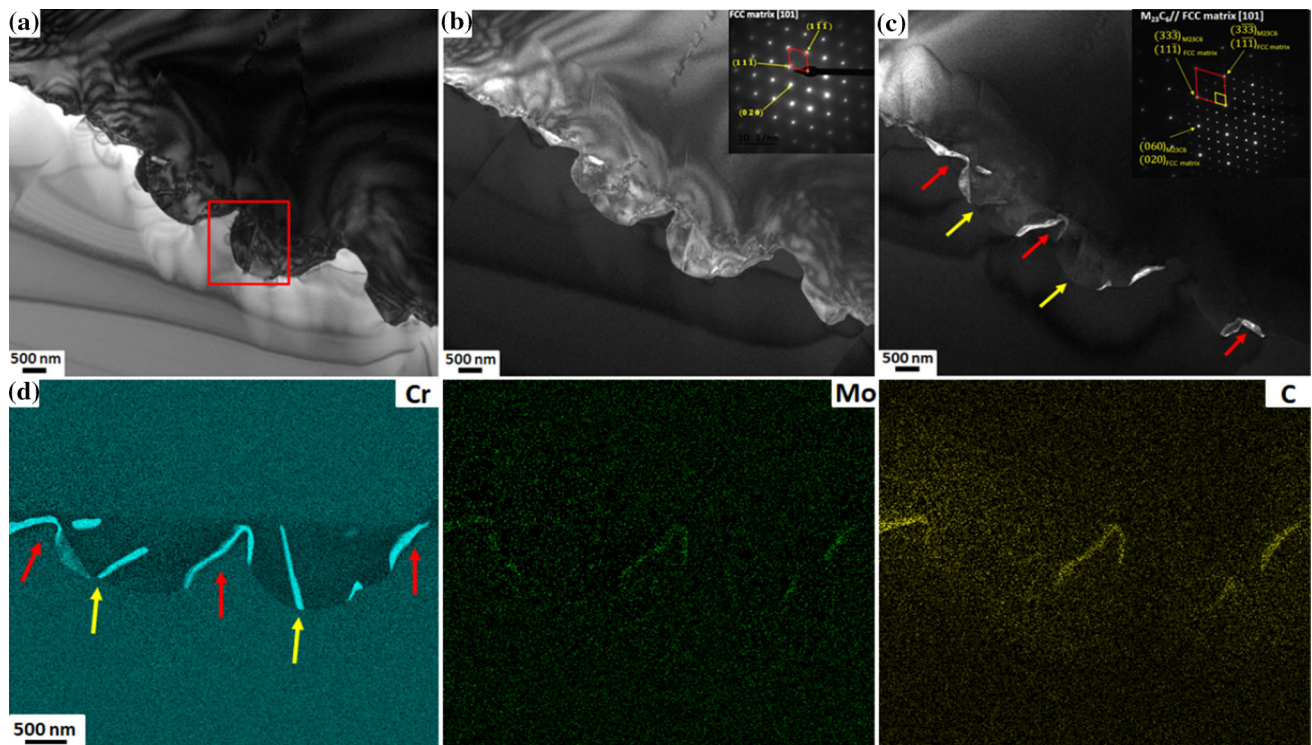
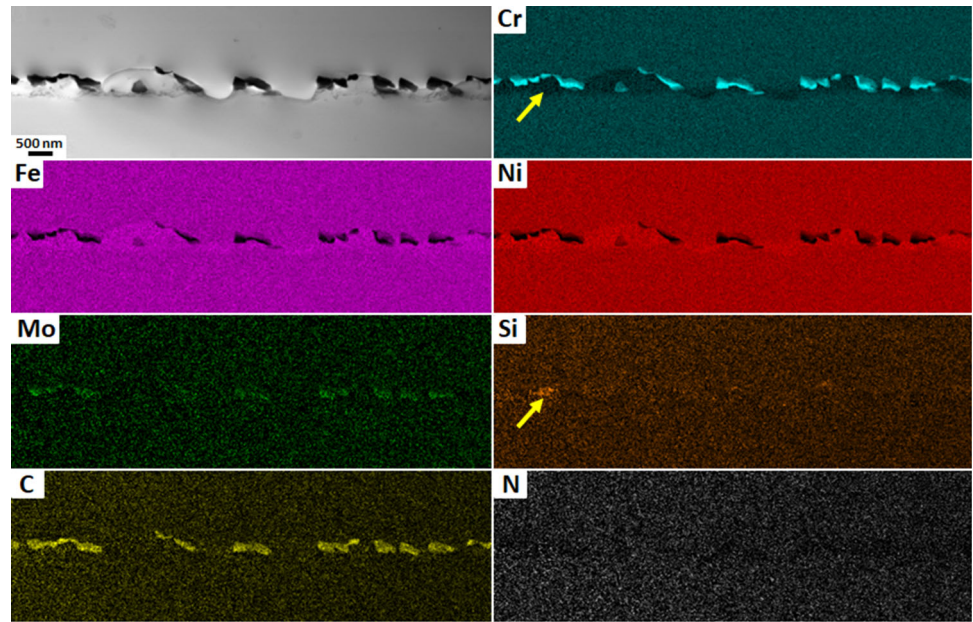


Figure 8 **a** BF-TEM image of GB migrated in Alloy 33 aged at 800 °C for 1 h; **b** respective CDF-TEM image and corresponding SAED pattern obtained from the upper grain in **a**; **c** CDF-TEM image of $M_{23}C_6$ at the GB. Inset in **c**: SAED pattern obtained from

the $M_{23}C_6$ /FCC matrix interface, $z = [101]_{M_{23}C_6} \parallel [101]_{FCC\ matrix}$; and **d** XEDS maps of Cr, Mo, and C obtained from the precipitation products associated with the migrated GB.

yellow arrows in Fig. 8c. XEDS maps shown in Fig. 8d confirm the difference on the chemical composition between these two precipitated phases. The $M_{23}C_6$ is enriched in Cr, Mo, and C (red arrows in

Fig. 8d), whereas the α -Cr phases are rich in Cr (yellow arrows in Fig. 8d). Figure 9 contains complementary BF and DF TEM images obtained from the region indicated by the red box in Fig. 8a. From

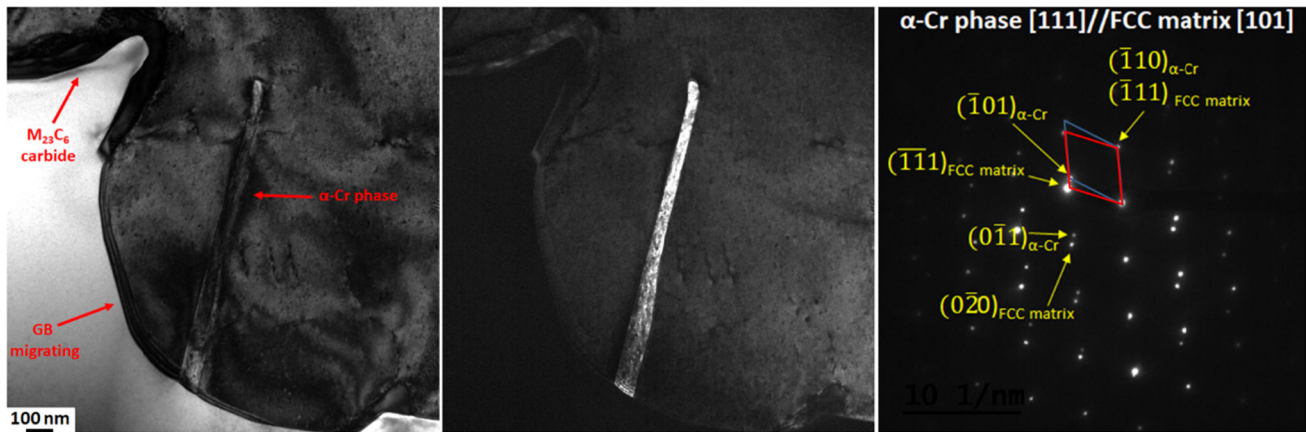


Figure 9 a Complementary BF/CDF TEM images of lamellar precipitates resulting from aging at 800 °C for 1 h obtained from the region indicated by the red box in Fig. 8a, which were identified by SAED as α -Cr phase with a BCC structure. The α -Cr

phase exhibited a K.S. O.R. with the FCC matrix: $(\bar{1}10)_{\alpha\text{-Cr}} \parallel (\bar{1}11)_{\text{FCC matrix}}, [111]_{\alpha\text{-Cr}} \parallel [101]_{\text{FCC matrix}}$.

SAED pattern shown in Fig. 9c, it is possible to identify the lamellar precipitates as the α -Cr phase with BCC structure. A Kurdjumov-Sachs (K.S.) O.R. between the α -Cr phase and FCC matrix is identified as $(\bar{1}10)_{\alpha\text{-Cr}} \parallel (\bar{1}11)_{\text{FCC matrix}}, [111]_{\alpha\text{-Cr}} \parallel [101]_{\text{FCC matrix}}$, which was also reported by other authors [54–56]. Such α -Cr phase with BCC structure in heterogeneous and homogeneous morphology has been found in several multicomponent structural alloys, such as Ni-based alloys [55–59] and stainless steel [60, 61]. However, lamellae of the α -Cr phase that has constituted DP colonies have only been reported to form in binary Ni–Cr alloys [62].

A BF-STEM image of intergranular precipitates with locally bowed/migrated grain boundary regions formed during aging at 800 °C for 2 h is shown in Fig. 10. In contrast to the observations at other boundaries, in this example, the migrated GB was connected with the tip of the precipitate (indicated by the red arrows) in some regions, whereas in others regions, the boundary had migrated without connection to the precipitates (indicated by the black arrows). The latter behaviour may indicate that the boundary migration was not influenced by the precipitate growth, but rather that the DIGM phenomenon has dominated. This phenomenon occurs if interdiffusion of two chemically different species along the GB induces a transverse shift of the boundary [13, 63]. In general, it was observed that DIGM does not occur at all GBs in the alloy, which confirms that GB thermokinetic properties depend on the individual GB structure [64, 65]. In fact, Hillert

and Purdy [13] have pointed out the close relation of the DIGM phenomenon to the DP reaction.

Figure 10b shows the elemental maps extracted from the STEM-XEDS SI dataset acquired from the region indicated by the yellow box in Fig. 10a. As seen in the previous figures, Cr-depletion and Ni–Fe-enrichments were observed in the region behind the migrated boundary. Moreover, all GB precipitates were Cr-rich and enriched in Mo, but some exhibited local Si- and N-enrichments, suggesting a nitride. As expected, GB precipitates containing Cr–Mo–C were identified by SAED patterns as Cr-rich $M_{23}C_6$. The Si-enriched precipitates were located adjacent to the Cr-rich $M_{23}C_6$. The SAED patterns obtained from the Si-enriched features were similar to $M_{23}C_6$, but detailed analysis confirmed that the structure was diamond-cubic.

The microstructure developed in Alloy 33 after aging at 800 °C for 5 h is shown in the BF-TEM image of Fig. 11. Several precipitates at original GB position are observed. Two arrowed precipitates are located at the original GB position, pinning its migration, and two other precipitates have formed within the depleted matrix swept by the migrating boundary. A further significant observation was the formation of a plate-like precipitate at DP reaction front, which possibly occurred after GB migration. This precipitate shown in the CDF-TEM image of Fig. 12a was identified as σ -phase with tetragonal structure from the SAED pattern (Fig. 12b), which was also observed at DP reaction front by other authors in austenitic stainless steels [21, 23, 24]. The XEDS maps indicated

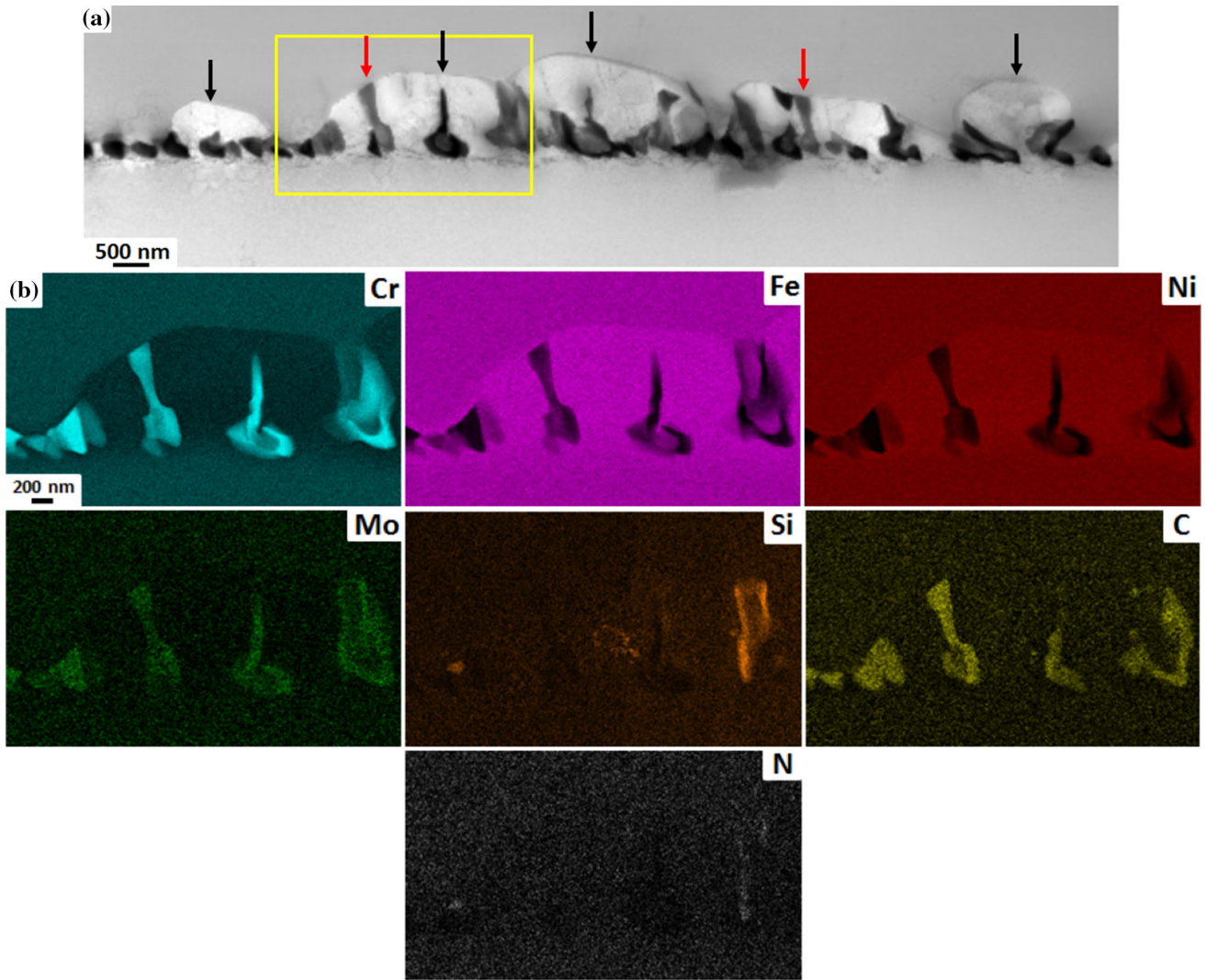


Figure 10 **a** BF-STEM image of precipitates at the migrated GB, which represents the earlier stages of DP reaction in Alloy 33 aged at 800 °C for 2 h, and **b** STEM-XEDS maps of Cr, Fe, Ni, Mo, Si, C, and N obtained from the region indicated by yellow box in **a**.

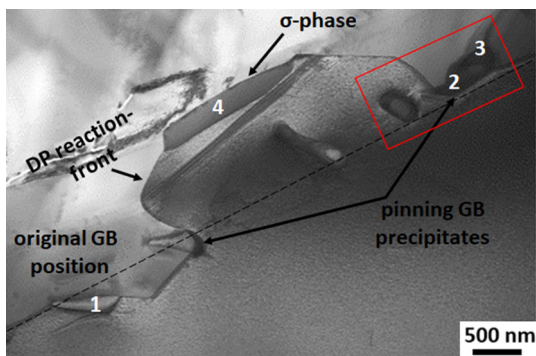


Figure 11 BF-STEM image of GB precipitates in Alloy 33 aged at 800 °C for 5 h. The dotted line indicates the original GB position.

this plate-like σ -phase was enriched in Cr and Mo but also contained Fe, Si, and Ni, as shown in Fig. 13.

In order to identify the nature of the above-mentioned GB precipitates, the region indicated by the red box in Fig. 11 was analysed in more detail by means of STEM techniques as shown in Fig. 14. Figure 14 shows a HAADF-STEM image. The XEDS maps of Cr, Fe, Ni, Mo, Si, N, and C revealed the existence of three different precipitates in this specific region of the DP colony, as follows: (1) Cr-rich precipitate in the region behind the migrated boundary, which was identified by electron diffraction as α -Cr phase with BCC structure; (2) a Cr–Mo–C-enriched precipitate ($M_{23}C_6$) at the triple point, and (3) Si–Mo–Ni–N–Cr-enriched precipitate also at the triple point.

Figure 12 **a** CDF-TEM image of a σ -phase precipitate observed at DP reaction front in the colony shown in Fig. 11, and **b** the corresponding [1 1 3] SAED pattern.

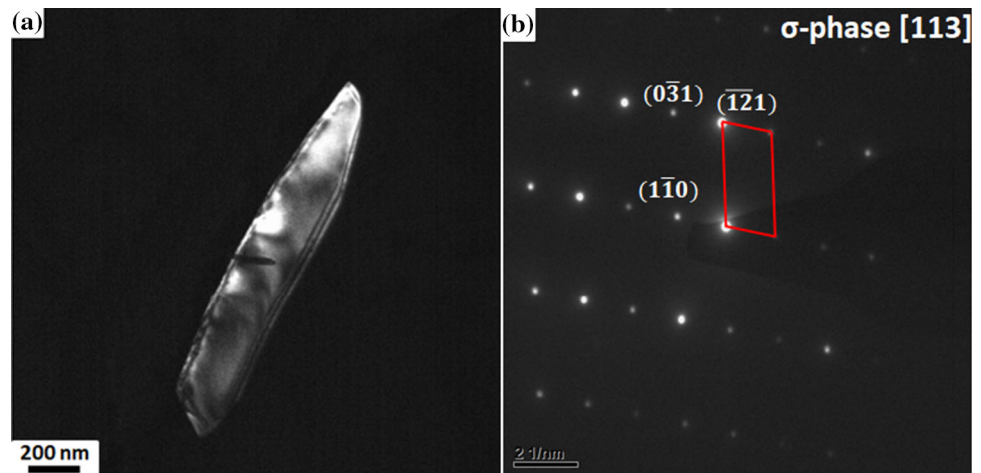
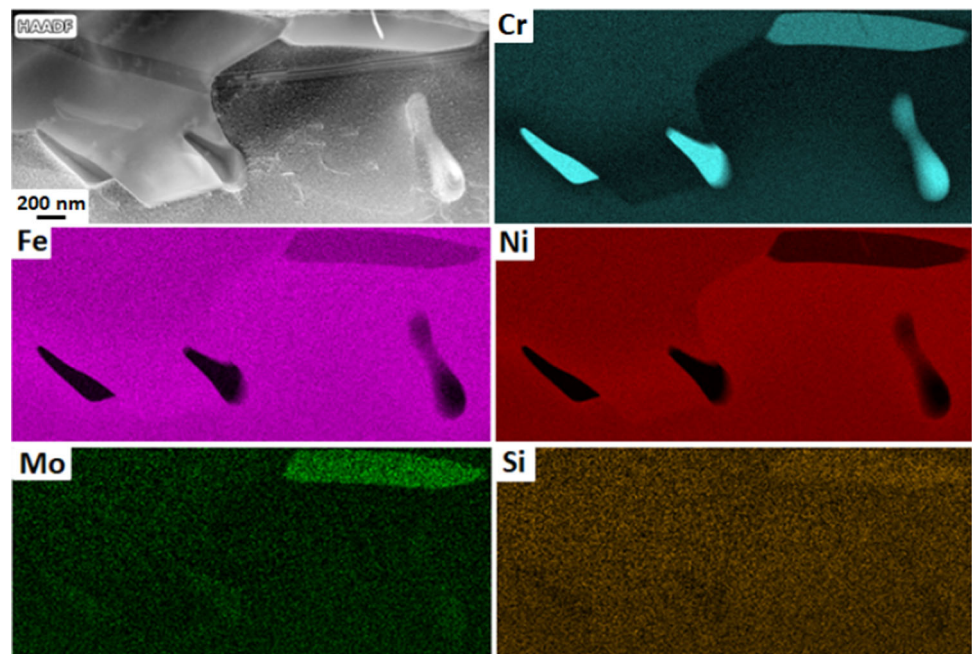


Figure 13 HAADF-STEM image obtained from the precipitation product at GB shown in Fig. 11 and corresponding XEDS maps of Cr, Fe, Ni, Mo, and Si extracted from the STEM-XED-SI dataset.

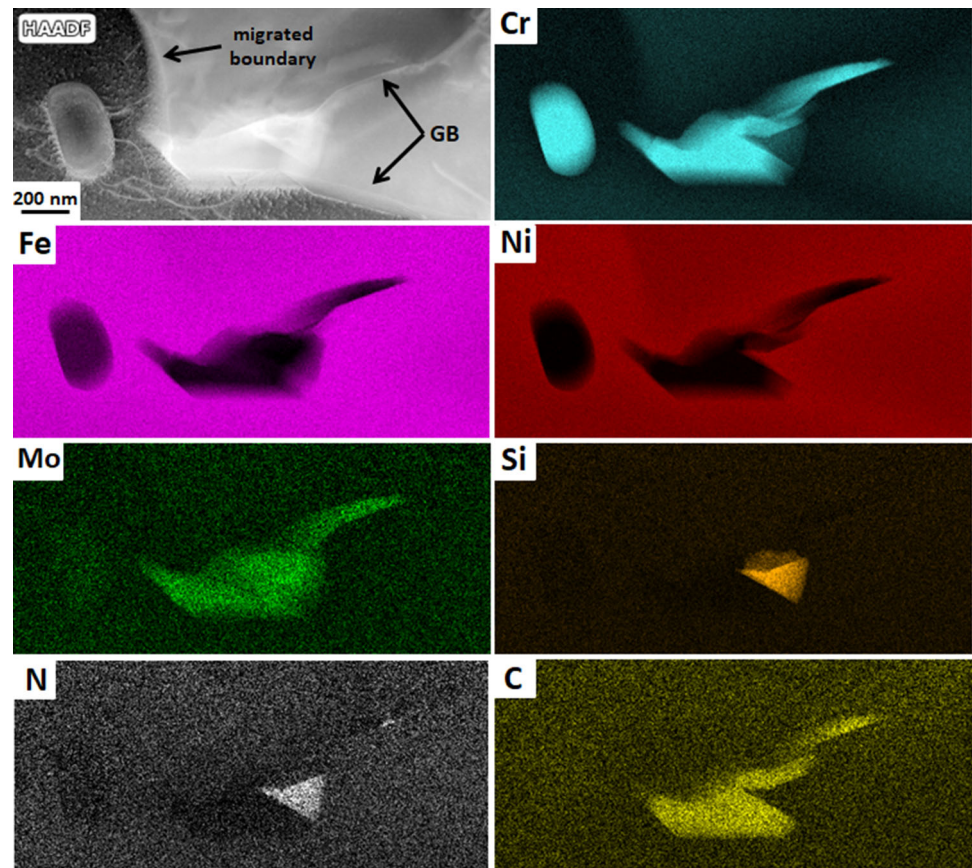


It is noted that the Si-enriched phase in this boundary formed adjacent to the $M_{23}C_6$. In addition, XED spectra were obtained from the precipitates indicated by the labels 1–4 in Fig. 11, confirming the existence of four different precipitated phases, which are shown in Fig. 15. Spectrum 1 was obtained from the α -Cr rich phase, although low levels of Fe, Mo, and Ni were also present. Spectrum 2 was obtained from the $M_{23}C_6$ at triple point, which was rich in Cr, but also enriched in Mo, Ni, and Fe. The low peak of Si in both spectra 1 and 2 may be associated with the matrix or due to Si internal fluorescence peak from the XEDS detector [66]. Spectrum 3 was obtained from the nitride, which was enriched in Si, Ni, Cr,

Mo, and N. Low levels of Fe and V (not reported in the chemical composition of the alloy) were also detected in the XED spectrum. Spectrum 4 was obtained from the σ -phase enriched in Cr and Mo, but containing Fe, Ni, and low levels of Si. This specific DP colony (shown in Fig. 11) exhibited different characteristics when compared with the majority of the colonies observed in this work. In general, the dominant intergranular precipitate was $M_{23}C_6$, but in this DP colony, the α -Cr phase had precipitated at original position of the GB prior to boundary migration.

Figure 16 shows a HAADF-STEM image of a typical example of DP colony observed in Alloy 33 aged

Figure 14 HAADF-STEM image obtained from the region indicated by the red box in Fig. 11 and corresponding XEDS maps of Cr, Fe, Ni, Mo, Si, N, and C extracted from the STEM-XEDS-SI dataset.



at 800 °C for 10 h. This colony contained a chain of precipitates at the original GB position and lamellar precipitates growing into the opposite grain, also observed by Portella et al. [45]. STEM-XEDS maps obtained from this DP colony confirmed that all precipitates behind the migrated boundary were Cr-rich. Three different precipitates were identified in this DP colony: (1) irregular Cr–Mo-enriched $M_{23}C_6$ at the original GB position; (2) BCC α -Cr phase lamellar precipitates; and (3) irregular Si–Mo–Cr-enriched precipitates formed at the original GB position and within of DP colony. Yen et al. [67] have observed colonies constituted by Cr-rich α -phase in a Fe-40 wt% Cr-40 wt% Ni ternary alloy aged at 750 °C for 720 h.

Si-enriched precipitates, such as G-phase [48–50, 60, 61, 68–71], H-phase [72, 73], and M_6X ($X = C$ and/or N) [47, 49, 50, 69, 74–84], have already been reported in several types of structural alloys. However, Maziasz [85] claimed H-phase should be referred to as eta-phase (M_6X). The following arguments are pertinent to discussion on these Si-rich phases. G-phase (FCC structure) and M_6X (cubic-

diamond structure) with lattice parameter in a range of 1.06–1.24 nm have been reported in several types of structural alloys, such as steel [72], aged stainless steels [47, 60, 61, 68, 73, 74, 77, 78, 82], irradiated austenitic stainless steels [49, 50, 69, 70, 74, 75], and Ni-based alloys [71, 83]. The chemical composition of both the above-mentioned Si-enriched phases may vary depending on the alloy system and the condition of the material [48–50, 60, 61, 68–70, 73–76, 78, 80, 81, 86]. For example, the Si content on the G-phase has been reported to vary in a range of 14–41 at.% depending on the chemical composition and conditions of the alloy [48, 50, 60, 61, 70].

Due to the significant variation in chemical composition of Si-enriched precipitates reported in the literature, phase identification requires electron diffraction to confirm the crystal structure. Depending on the zone axis, both G-phase (FCC structure) and M_6X (diamond-cubic structure) may generate similar SAED patterns for certain zone axes. However, electron diffraction patterns from the diamond-cubic structure in [001] zone axis can be distinguished from FCC structure. This difference between

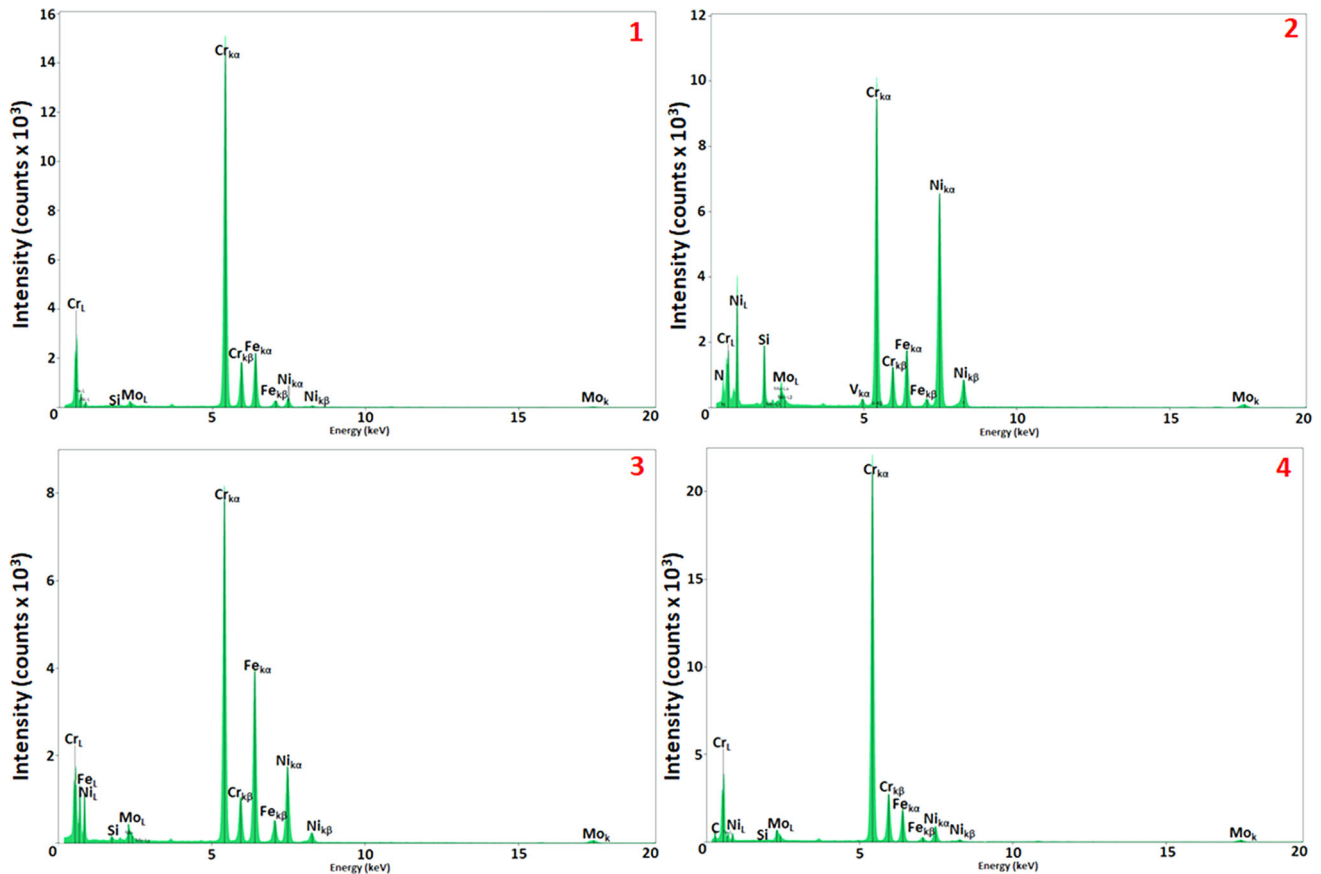


Figure 15 XED spectra obtained from the precipitates labelled 1, 2, 3, and 4 in Fig. 11. 1 α -Cr phase (BCC structure); 2 $M_{23}C_6$ (FCC structure); 3 Si-enriched precipitate; 4 σ -phase (tetragonal structure).

diamond-cubic and FCC structure is due to the structure factor of diamond-cubic to predict systematic absences of (200), (420) reflections that are present for the FCC structure [50, 69].

Figure 17a shows a HAADF-STEM image obtained from the region indicated by the red box in Fig. 16 showing GB precipitates at original GB position and part of the lamellar DP precipitate of α -Cr phase. XEDS maps of Cr, Fe, Ni, Si, and Mo in this figure clearly show the compositional differences between the distinct types of precipitates. The various phases were identified via electron diffraction as shown in Fig. 17: the [001] SAED patterns were obtained from the FCC matrix (Fig. 17b), FCC $M_{23}C_6$ (Fig. 17c), and the Si-enriched phase (Fig. 17d). As expected, the intergranular precipitate shown in Fig. 17a was identified as Cr-rich $M_{23}C_6$ with FCC structure. However, the Si-enriched precipitates observed in Alloy 33 aged at 800 °C for 10 h were confirmed to be the M_6N with a diamond-cubic structure. (This phase identified as M_6N has been

labelled as eta-phase in a previous publication [44].) As observed in Fig. 17 in which all diffraction patterns were obtained from the [001] zone axis, the [001] SAED pattern from the Si-enriched phase exhibits clear differences from that of the [001] FCC $M_{23}C_6$. In the former, some forbidden reflections have been verified, which confirmed the diamond-cubic structure of the Si-enriched phase. Both Cr-rich $M_{23}C_6$ and Si-enriched M_6N have a cube-on-cube OR with the FCC matrix. Based on these observations, the Si-enriched phases formed both at the original GB position and within the DP colony are the M_6N with diamond-cubic structure. The M_6X phase has been reported as carbides (M_6C) [47, 49, 50, 69, 76, 82–84], nitrides (M_6N) [77], or carbonitrides ($M_6(CN)$) [78, 81] depending on the chemical composition of the alloy, but in general, it is enriched in Si, Ni, and Cr, in addition to Fe, Mo, and V [49, 50, 69, 73–76, 78, 81], as shown in this investigation.

Although the semi-quantitative XEDS results from the precipitates identified in the present work

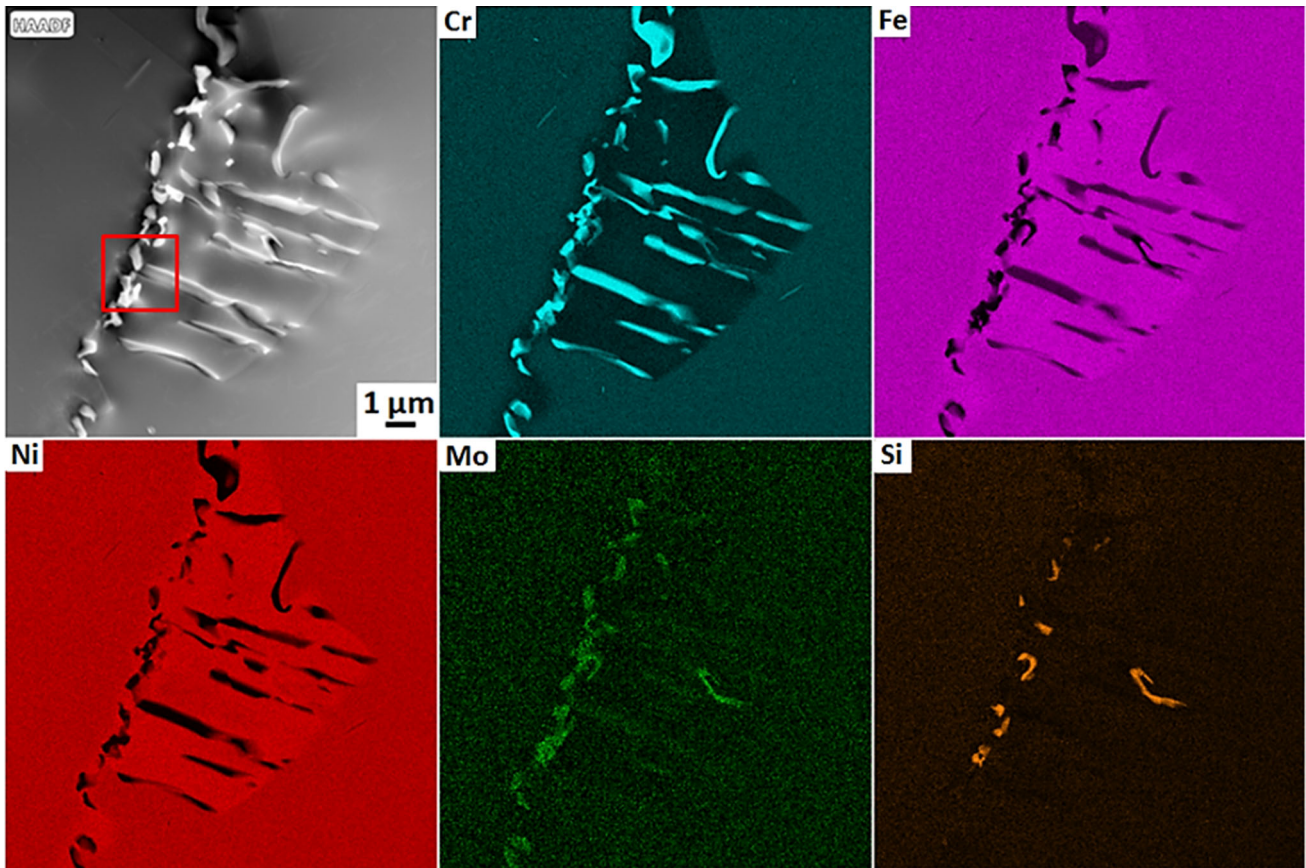


Figure 16 HAADF-STEM image of DP colony in Alloy 33 aged at 800 °C for 10 h and corresponding XEDS maps of Cr, Fe, Ni, Mo, and Si extracted from the STEM-XED-SI dataset.

(Table 2) are similar to those reported in other studies addressing precipitated phase identification in multicomponent structural alloys [47, 74, 78, 81, 87–90], these results provide a comparison between the different precipitates identified in this investigation. As shown in Table 2, there is little scatter in the chemical composition of both the $M_{23}C_6$ (1 h and 2 h) and α -Cr phase (1 h and 10 h). On the other hand, the results obtained from the $M_{23}C_6$ and M_6N after 10 h of aging showed significant variations in alloy elements concentrations. Such differences could be attributed to stray EDS signals generated from the matrix around the precipitates under analysis by the electron probe in different thin foil TEM samples.

It is worth noting that the semi-quantitative XEDS values shown in Table 2 may serve as a reference for the identification of the different precipitated phases in the present investigation. As observed, $M_{23}C_6$ was distinguished from the M_6N (besides the electron diffraction results) because of the amount of Cr, Ni, and Si analysed. Although the former ($M_{23}C_6$) had

higher quantity of Cr and no Si, the latter (M_6N) contains more Ni–Si and lower Cr when compared with the $M_{23}C_6$. Moreover, the BCC Cr-rich α -phase contained some Fe and a limited amount of Ni and Mo. In addition, the Fe/Ni ratio verified in both the $M_{23}C_6$ and α -Cr phase can be a useful parameter to differentiate these two precipitated phases observed in this investigation.

One can argue that M_6N was frequently adjacent to the $M_{23}C_6$ at original GB position, as can be seen in Fig. 17. However, the precipitation of M_6N within the DP colony contradicts the idea that this Si-enriched phase only formed in association with $M_{23}C_6$. The M_6N within the colony shown in Fig. 16 had precipitated adjacent to a lamellar discontinuous α -Cr precipitate, which confirmed that the M_6N was not always associated with the carbide. This suggests that M_6N can nucleate and grow in association with either $M_{23}C_6$ or α -Cr phase due to the local enrichment of the matrix in Si, Ni, and N adjacent to these

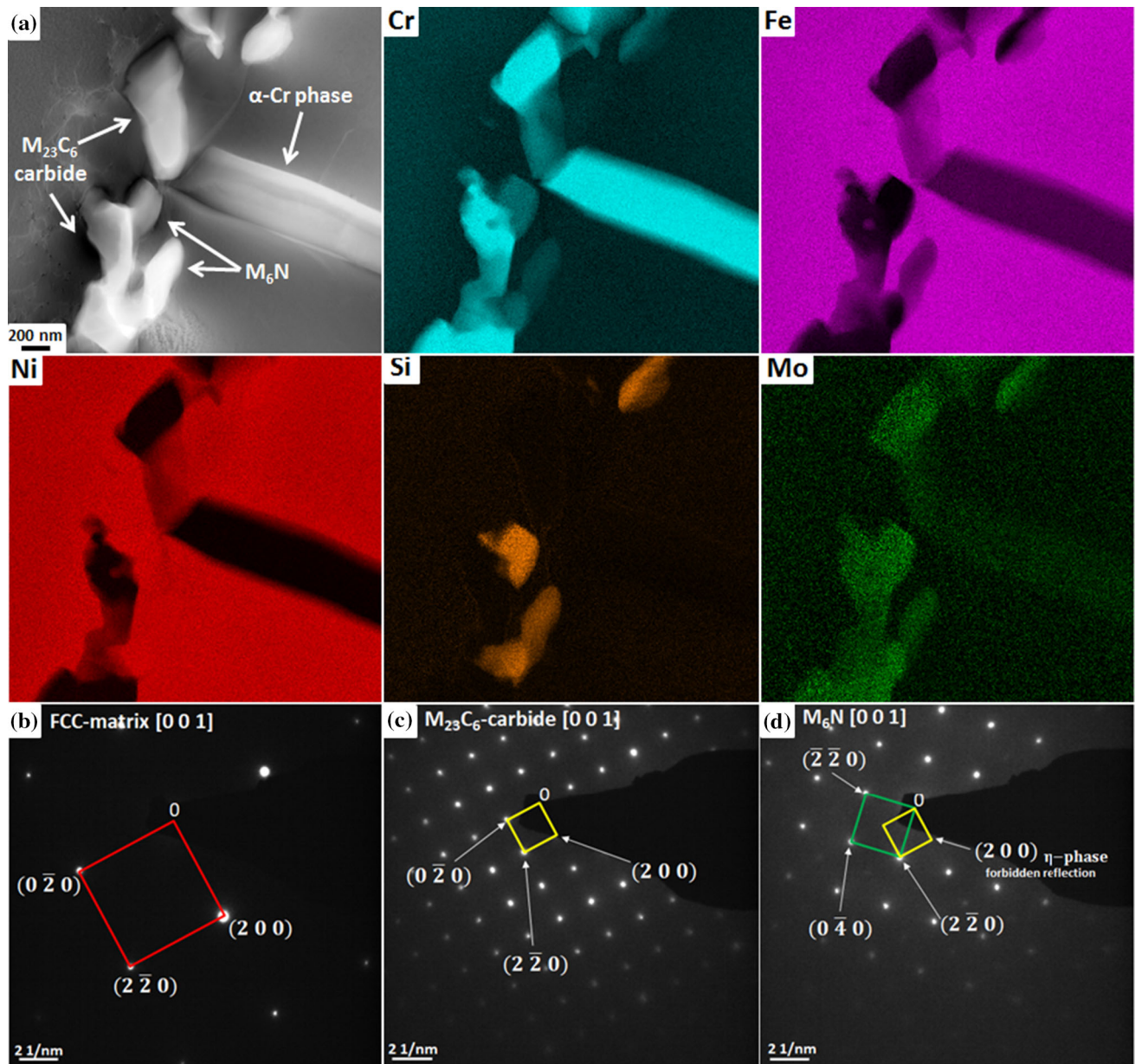


Figure 17 a HAADF-STEM image of Alloy 33 aged at 800 °C for 10 h obtained from the region indicated by the red box in Fig. 16 and corresponding XEDS maps of Cr, Fe, Ni, Si, and Mo;

and respective [001] SAED patterns for b FCC-matrix, c $M_{23}C_6$, and d Si-enriched M_6N .

precipitates as these elements have little or no affinity with the $M_{23}C_6$ and α -Cr phase [91].

Studies of DP initially focused on binary alloys containing only substitutional solutes. There has been considerable research concerning the proposed mechanism for initiation of DP [12, 46, 92, 93] as well as models for growth kinetics [15, 94–98]. However, in multicomponent systems containing substitutional and interstitial atoms that have orders of magnitude differences in atomic diffusivities, there are also a

number of differences in structural and kinetic characteristics. In particular, the difference in chemical composition plays a major role in the discontinuous reaction [7, 20, 22, 23, 25–28]. In binary alloy systems, it is possible to model the steady-state growth of the DP reaction [5, 17], whereas the same conditions do not apply to multicomponent alloy systems due to the additional complexity associated with substitutional and interstitial solutes [23, 24]. However, one characteristic is common in all binary and

Table 2 Semi-quantitative STEM/XEDS analyses (normalized) of precipitates in Alloy 33 after isothermal aging at 800 °C from 1 to 10 h^a

Type of precipitate ^b	Aging time (h)	Cr	Fe	Ni	Mo	Si	V
M ₂₃ C ₆ (11)	1	80.8 ± 1.5	8.0 ± 0.7	4.7 ± 0.9	6.0 ± 1.1	0.6 ± 0.5	
M ₂₃ C ₆ (8)	2	78.6 ± 1.8	8.1 ± 1.2	4.6 ± 1.0	6.8 ± 1.1	2.0 ± 1.3	
α-Cr phase (3)	1	76.9 ± 1.8	13.7 ± 1.1	3.4 ± 0.1	2.8 ± 0.8	3.2 ± 2.0	
α-Cr phase (31)	10	80.7 ± 1.2	13.3 ± 0.6	2.6 ± 0.6	3.0 ± 0.6	0.4 ± 0.2	
M ₆ N (9)	10	44.4 ± 7.4	12.1 ± 7.7	31.4 ± 4.9	6.1 ± 2.1	5.2 ± 2.5	0.7 ± 3

^aNumbers in parentheses denote the number of discrete analyses quantified using the standardless Cliff–Lorimer technique

^bThe statistical variations reported here represent particle-to-particle variations

multicomponent systems undergoing DP reported in the literature: the precipitated phase at the original GB position grows together with the migrating GB to become the main precipitated phase within the DP colony, i.e. the discontinuous precipitates.

Moreover, an unusual form of DP colonies observed in multicomponent systems has been reported in Ni-based alloys with a biphasic-supersaturated matrix in which the DP colony contained 3 different phases [37–39]. In this type of DP reaction, the metastable biphasic microstructure transforms into a cellular structure containing 3 different phases. As in DP constituted of carbides and nitrides, the precipitates within this unusual colony can occur as lamellar and discrete particles [37, 39]. An additional complexity in the occurrence of DP in multicomponent alloys was confirmed in the present work in which the first precipitated phase formed at GB was FCC M₂₃C₆. However, based on the classical DP theory, the precipitates at GB should grow in a lamellar morphology and constitute the DP colony. Thus, it was expected that the intergranular M₂₃C₆ would grow together with the migrating GB, but in Alloy 33, the discontinuous precipitates are the BCC α-Cr phase. In general, the development of the DP colonies in Alloy 33 aged at 800 °C can be summarized in the following four stages: (1) initial precipitation of Cr-rich M₂₃C₆ at GBs in the early stages of aging; (2) local migration of some parts of the GB adjacent to the M₂₃C₆; (3) growing of α-Cr phase with lamellar morphology behind the migrating boundary and heterogeneous precipitation of Si-enriched M₆N associated with either M₂₃C₆ at original GB position or α-Cr phase within the DP colony; and (4) as the aging time increase, α-Cr phases nucleated adjacent to M₂₃C₆ at the migrating GB grow as lamellar precipitates into the FCC grain. In particular, for Alloy

33, the α-Cr phase grows along with the migrating GB as opposed to M₂₃C₆, which has usually been identified as the main discontinuous phase in other Ni-based alloys and austenitic stainless steels undergoing discontinuous reactions phenomena.

Conclusions

A detailed microstructural investigation of the DP reactions in Alloy 33 resulting from isothermal aging at 800 °C for 1 up to 10 h was successfully conducted. To the authors' knowledge, this is the first study that shows the evolution of DP reactions in this alloy system together with the identification of the precipitated phases within the DP colonies. Specific findings include the following:

1. The DIGM phenomenon has been observed to occur both an isolated and preceding development of DP colonies. At this temperature, the migration of the boundary upon aging could proceed to one side or both sides of the boundary.
2. STEM-XED spectrum imaging analyses and electron diffraction confirmed that DP colonies are generated by solute partitioning within the colony resulting in the formation of three different phases precipitated constituting the same DP colony: Cr-rich M₂₃C₆ precipitation occurred at the original GB position; this was followed by precipitation of Si-enriched M₆N at the GB and α-Cr phase behind the migrating boundary. With increasing aging time, α-Cr phases nucleated adjacent to the GB grew as lamellar precipitates. Eventually, M₆N formed within the colony along with σ-phase at the DP reaction front.
3. The FCC Cr-rich M₂₃C₆ and diamond cubic M₆N exhibit a cube-on-cube O.R. with the FCC matrix:

$(001)_{M_{23}C_6} \parallel (001)_{FCC \text{ matrix}}$; $[001]_{M_{23}C_6} \parallel [001]_{FCC \text{ matrix}}$.
The BCC α -Cr discontinuous lamellar precipitates exhibit a Kurdjumov-Sachs O.R. with the FCC matrix: $(\bar{1}10)_{\alpha\text{-Cr}} \parallel (\bar{1}11)_{FCC \text{ matrix}}$, $[111]_{\alpha\text{-Cr}} \parallel [101]_{FCC \text{ matrix}}$.

4. The microstructural evolution during aging at 800 °C indicates that the nature of the DP reaction in Alloy 33 differs from the classical DP theory, which predicts that the precipitate initially formed at GB (Cr-rich $M_{23}C_6$) grows together with the GB migration. However, as shown in this work, the discontinuous precipitates (α -Cr phase) have nucleated adjacent to GB and grown in association with the migrating GB and not at the original GB position.

Acknowledgements

This research was sponsored by the Brazilian Funding Agencies—CAPES (Grant Number 001) and CNPQ (Grant Number 204921/2017–1) and NSF/MWN (US: DMR-0303429) joint CNPq/CIAM Program. M.G. Burke acknowledges the financial support of the UK Engineering and Science Research Council through Grant EP/N017854/1. The authors are grateful to Brazilian Center for Research in Physics (CBPF-Brazil) for the access to the LABNANO Electron Microscopy facilities. Thanks are due to Dr. P.D. Portella (BAM, Germany) for providing the alloy studied here.

Funding

This study was funded by the Brazilian Funding Agencies—CAPES (grant number 001) and CNPQ (grant number 204921/2017–1) and NSF/MWN (US: DMR-0303429) joint CNPq/CIAM Program. M.G. Burke acknowledges the financial support of the UK Engineering and Science Research Council through Grant EP/N017854/1.

Compliance with ethical standards

Conflict of interest The authors declare that they have no conflict of interest.

References

- [1] Butler EP, Burke MG (1986) Chromium depletion and martensite formation at grain boundaries in sensitised austenitic stainless steel. *Acta Metall* 34:557–570
- [2] Simmons JW (1995) Mechanical properties of isothermally aged high-nitrogen stainless steel. *Metall Mater Trans A* 26:2579–2595
- [3] Merrick HF, Hayden HW, Gibson RC (1973) The effect of carbon and titanium on the hot workability of 25Cr-6Ni stainless steels. *Metall Trans* 4:827–832
- [4] Raymond EL (1968) Mechanisms of sensitization and stabilization of INCOLOY nickel-iron-chromium alloy 825. *Corrosion* 24:180–188
- [5] Manna I, Pabi SK, Gust W (2001) Discontinuous reactions in solids. *Int Mater Rev* 46:53–91
- [6] Lee T, Kim S, Takaki S (2006) Time-temperature-precipitation characteristics of high nitrogen austenitic Fe–18Cr–18Mn–2Mo–0.9N steel. *Metall Mater Trans A* 37:3445–3454
- [7] Kikuchi M, Kajihara M, Choi S-K (1991) Cellular precipitation involving both substitutional and interstitial solutes: cellular precipitation of Cr_2N in Cr–Ni austenitic steels. *Mater Sci Eng A* 146:131–150
- [8] Vanderschaeve F, Taillard R, Foct J (1995) Discontinuous precipitation of Cr_2N in a high nitrogen, chromium-manganese austenitic stainless steel. *J Mater Sci.* 30(6035):6046. <https://doi.org/10.1007/BF01151525>
- [9] Langelier B, Persaud SY, Korinek A, Casagrande T, Newman RC, Botton GA (2017) Effects of boundary migration and pinning particles on intergranular oxidation revealed by 2D and 3D analytical electron microscopy. *Acta Mater* 131:280–295
- [10] Bertali G, Scenini F, Burke MG (2016) The effect of residual stress on the Preferential Intergranular Oxidation of Alloy 600. *Corros. Sci.* 111:494–507
- [11] Shen Z, Meisnar M, Arioka K, Lozano-Perez S (2019) Mechanistic understanding of the temperature dependence of crack growth rate in alloy 600 and 316 stainless steel through high-resolution characterization. *Acta Mater* 165:73–86
- [12] Solorzano IG, Lopes MFS (1988) Diffusion-induced grain boundary migration as precursor of discontinuous precipitation in Al–Zn alloys. *Phase Transform* 87:242–245
- [13] Hillert M, Purdy GR (1978) chemically induced grain boundary migration. *Acta Metall* 26:333–340
- [14] Hillert M (1972) On theories of growth during discontinuous precipitation. *Metall Trans* 3:2729–2741
- [15] Cahn JW (1959) The kinetics of cellular segregation reactions. *Acta Metall* 7:18–28

- [16] Solorzano IG, Purdy GR, Weatherly GC (1984) Studies of the initiation, growth and dissolution of the discontinuous precipitation product in aluminium–zinc alloys. *Acta Metall* 32:1709–1717
- [17] Williams DB, Butler EP (1981) Grain boundary discontinuous precipitation reactions. *Int Mater Rev* 26:153–183
- [18] Ainsley MH, Cocks GJ, Miller DR (1979) Influence of grain boundary structure on discontinuous precipitation in austenitic steel. *Met Sci* 13:20–24
- [19] Kikuchi M, Urabe T, Cliff G, Lorimer GW (1990) The loss of driving force due to volume diffusion ahead of a migrating boundary in a cellular precipitation reaction. *Acta Metall Mater* 38:1115–1120
- [20] Hillert M, Lagneborg L (1971) Discontinuous precipitation of $M_{23}C_6$ in austenitic steels. *J Mater Sci.* 6(208):212. <https://doi.org/10.1007/BF00550014>
- [21] Lee T-H, Ha H-Y, Kim S-J (2011) precipitation of second phases in high-interstitial-alloyed austenitic steel. *Metall Mater Trans A* 42:3543–3548
- [22] Presser R, Silcock JM (1983) Aging behaviour of 18Mn–18Cr high nitrogen austenitic steel for end rings. *Met Sci* 17:241
- [23] Knutsen RD, Lang CI, Basson JA (2004) Discontinuous cellular precipitation in a Cr–Mn–N steel with niobium and vanadium additions. *Acta Mater* 52:2407–2417
- [24] Lee T-H, Oh C-S, Lee CG, Kim S-J, Takaki S (2004) Precipitation of σ -phase in high-nitrogen austenitic 18Cr–18Mn–2Mo–0.9N stainless steel during isothermal aging. *Scr Mater* 50:1325–1328
- [25] Zheng L, Hu X, Kang X, Li D (2015) Precipitation of $M_{23}C_6$ and its effect on tensile properties of 0.3C–20Cr–11Mn–1Mo–0.35N steel. *Mater Des* 78:42–50
- [26] Rayaprolu DB, Hendry A (1989) Cellular precipitation in a nitrogen alloyed stainless steel. *Mater Sci Technol* 5:328–332
- [27] Carosi A et al (2010) Heating modification of an austenitic steel with high-nitrogen content. *Surf Interface Anal* 42:726–729
- [28] Voice WE, Faulkner RG (1987) The discontinuous precipitation of $M_{23}C_6$ in Nimonic 80A. *J Mater Sci* 22(4221):4232. <https://doi.org/10.1007/BF01132012>
- [29] Angeliu TM, Was GS (1990) Behavior of grain boundary chemistry and precipitates upon thermal treatment of controlled purity alloy 690. *Metall Trans A* 21:2097–2107
- [30] Shaikh MA, Iqbal M, Ahmad M, Akhtar JI, Shoaib KA (1992) Precipitation study of heat-treated Incoloy 825 by scanning electron microscopy. *J Mater Sci Lett* 11:1009–1011
- [31] Lim YS, Kim JS, Kim HP, Cho HD (2004) The effect of grain boundary misorientation on the intergranular $M_{23}C_6$ carbide precipitation in thermally treated Alloy 690. *J Nucl Mater* 335:108–114
- [32] Tavassoli AA, Colombe G (1977) On the creep ductility decline of alloy 800. *Scr Metall* 11:191–192
- [33] Tavassoli AA, Colombe G (1978) Mechanical and microstructural properties of alloy 800. *Metall Trans A* 9:1203–1211
- [34] Carvalho PA, Machado IF, Solorzano G, Padilha AF (2008) On Cr_2N precipitation mechanisms in high nitrogen austenite. *Philos Mag* 88:229–242
- [35] Lim YS, Kim DJ, Hwang SS, Kim HP, Kim SW (2014) $M_{23}C_6$ precipitation behavior and grain boundary serration in Ni-based Alloy 690. *Mater Charact* 96:28–39
- [36] Zhang S et al (2018) Precipitation behavior and phase transformation mechanism of super austenitic stainless steel S32654 during isothermal aging. *Mater Charact* 137:244–255
- [37] Nystrom JD, Pollock TM, Murphy WH, Garg A (1997) Discontinuous cellular precipitation in a high-refractory nickel-base superalloy. *Metall Mater Trans A* 28:2443–2452
- [38] Pollock TM (1995) The growth and elevated temperature stability of high refractory nickel-base single crystals. *Mater Sci Eng B* 32:255–266
- [39] Heckl A, Cenanovic S, Göken M, Singer RF (2012) Discontinuous precipitation and phase stability in Re- and Ru-containing nickel-base superalloys. *Metall Mater Trans A* 43A:10–19
- [40] Köhler M, Heubner U, Eichenhofer K-W, and Renner M (1998) Nicrofer 3033—alloy 33: a new corrosion-resistant austenitic material for many applications. In: VDM report
- [41] Klöwer J, Rommerskirche I, Kolb-Telieps A, Köhler M (2000) Alloy 33—a new high strength austenitic alloy for marine applications. *Corros* 636:1–11
- [42] Elbakhshwan MS et al (2017) High-temperature oxidation of advanced FeCrNi alloy in steam environments. *Appl Surf Sci* 426:562–571
- [43] Younker I, Fratoni M (2016) Neutronic evaluation of coating and cladding materials for accident tolerant fuels. *Prog Nucl Energy* 88:10–18
- [44] Spadotto JC, Dille J, Watanabe M, Solórzano IG (2018) Grain boundary precipitation phenomena in an alloy 33 (Cr–Fe–Ni–N) subjected to direct-aging treatments (700 °C and 900 °C). *Mater Charact* 140:113–121
- [45] Portella PD, Köhler M, Renner M (1999) Investigation of microstructure and properties of a chromium-rich austenitic material with high nitrogen content. *Mater Sci Forum* 318–320:201–208
- [46] Fournelle R, Clark J (1972) The genesis of the cellular precipitation reaction. *Metall Trans* 3:2757–2767

- [47] Weiss B, Stickler R (1972) Phase instabilities during high temperature exposure of 316 austenitic stainless steel. *Metall Trans* 3:851–866
- [48] Goldschmidt HJ (1967) *Interstitial alloys*, 1st edn. Springer, New York
- [49] Williams TM, Titchmarsh JM, Arkell DR (1982) Void-swelling and precipitation in a neutron-irradiated, niobium-stabilised austenitic stainless steel. *J Nucl Mater* 107:222–244
- [50] Boothby RM, Harries DR, Williams TM (1983) Precipitation and void-swelling in nickel-manganese austenitic stainless steels. *J Nucl Mater* 115:16–24
- [51] Kuz'ma YB, Fedorov TF (1965) Phase equilibria in the system molybdenum—chromium—carbon. *Sov Powder Metall Met Ceram* 4:920–922
- [52] Williams TM, Titchmarsh JM (1981) Silicon-rich phases in austenitic alloys. *J Nucl Mater* 98:223–226
- [53] Tan XP et al (2018) Carbide precipitation characteristics in additive manufacturing of Co–Cr–Mo alloy via selective electron beam melting. *Scr Mater* 143:117–121
- [54] Miller C, Field R, Kaufman M (2018) Phase stability of γ' -Ni₂Cr and α -Cr in the Ni–Cr binary. *Acta Mater.* 157:1–10
- [55] Khan S, Singh JB, Verma A, Karri M (2017) Precipitation of a chromium-rich α -phase in Alloy 693 and its effect on tensile properties. *Mater Sci Eng A* 686:176–183
- [56] Semba H (2015) Development of boiler tubes and pipes for advanced USC power plants. *Tech Rep* 397:71–77
- [57] Sun F, Gu YF, Yan JB, Zhong ZH, Yuyama M (2016) Phenomenological and microstructural analysis of intermediate temperatures creep in a Ni–Fe-based alloy for advanced ultra-supercritical fossil power plants. *Acta Mater* 102:70–78
- [58] Tokairin T, Dahl KV, Danielsen HK, Grummen FB, Sato T, Hald J (2013) Investigation on long-term creep rupture properties and microstructure stability of Fe–Ni based alloy Ni-23Cr-7W at 700 °C. *Mater Sci Eng A* 565:285–291
- [59] Bi Z, Dong J, Zheng L, Xie X (2013) Phenomenon and mechanism of high temperature low plasticity in high-Cr nickel-based superalloy. *J Mater Sci Technol* 29:187–192
- [60] Miller MK, Bentley J, Brenner SS, Spitznagel JA (1984) Long term thermal aging of type Cf 8 stainless steel. *Le J Phys Colloq* 45:6
- [61] Vrinat M, Cozar R, Meyzaud Y (1986) Precipitated phases in the ferrite of aged cast duplex stainless steels. *Scr Metall* 20:1101–1106
- [62] Keskar N, Pattanaik AK, Mani Krishna KV, Srivastava D, Dey GK (2017) Kinetics and grain boundary selectivity of discontinuous precipitation in binary Ni–Cr alloy. *Metall Mater Trans A* 48:3096–3107
- [63] Balluffi RW, Cahn JW (1981) Mechanism for diffusion induced grain boundary migration. *Acta Metall* 29:493–500
- [64] Kim W, Meyrick G, Shewmon PG (1983) Diffusion induced boundary migration and discontinuous precipitation in copper alloys. *Scr Metall* 17:1435–1440
- [65] Rutter JW, Aust KT (1965) Migration of $\langle 100 \rangle$ tilt grain boundaries in high purity lead. *Acta Metall* 13:181–186
- [66] Williams DB, Carter CB (2009) *Transmission electron microscopy: a textbook for materials science*, vol 1–4. Springer, New York
- [67] Yen YW, Su JW, Huang DP (2008) Phase equilibria of the Fe–Cr–Ni ternary systems and interfacial reactions in Fe–Cr alloys with Ni substrate. *J Alloys Compd* 457:270–278
- [68] Powell DJ, Pilkington R, Miller DA (1988) The precipitation characteristics of 20% Cr/25% NiNb stabilised stainless steel. *Acta Metall* 36:713–724
- [69] Williams TM, Titchmarsh JM (1979) The occurrence of a silicon-rich phase of the M₆C type in neutron-irradiated FV548 steel. *J Nucl Mater* 87:398–400
- [70] Williams TM, Titchmarsh JM, Arkell DR (1979) A nickel- and silicon-rich phase in irradiated FV548 steel. *J Nucl Mater* 82:199–201
- [71] Shingledecker JP, Pharr GM (2012) The role of eta phase formation on the creep strength and ductility of inconel alloy 740 at 1023 K (750 °C). *Metall Mater Trans A* 43:1902–1910
- [72] Hughes H (1959) A new silicide in a 12 per cent chromium steel. *Nature* 183:1543
- [73] Tither SJ, Clark BR (1970) Precipitation of H phase in a high-silicon austenitic stainless steel. *Met Sci* 4:118–120
- [74] Maziasz PJ (1979) The formation diamond-cubic eta (η) phase in type 316 stainless steel exposed to thermal aging or irradiation environments. *Scr Metall* 13:621–626
- [75] Brager HR, Garner FA (1978) Swelling as a consequence of gamma prime (γ') and M₂₃(C, Si)₆ formation in neutron irradiated 316 stainless steel. *J Nucl Mater* 73:9–19
- [76] Leitnaker JM, Potter GA, Bradley DJ, Franklin JC, Laing WR (1978) The composition of eta carbide in hastelloy N after aging 10,000 h at 815 °C. *Metall Trans A* 9:397–400
- [77] Sourmail T, Bhadeshia HKDH (2005) Microstructural evolution in two variants of NF709 at 1023 and 1073 K. *Metall Mater Trans A* 36:23–34
- [78] Jargelius-Pettersson RFA (1993) Precipitation in a nitrogen-alloyed stainless steel at 850 °C. *Scr Metall Mater* 28:1399–1403
- [79] Shingledecker JP, Evans ND, Pharr GM (2013) Influences of composition and grain size on creep-rupture behavior of Inconel® alloy 740. *Mater. Sci. Eng. A* 578:277–286
- [80] Stadelmaier MM (1969) *Developments in the structural chemistry of alloy phases*, 1st edn. Springer, New York
- [81] Zhu Z, Cheng C, Liu C, Zhao J (2012) Microstructure evolution and nitridation in an As-Cast 25Cr-35Ni-1Mo

- radiant tube after long-term service. *Metall Mater Trans A* 43:4525–4531
- [82] Maziasz PJ et al (2007) Advanced alloys for compact, high-efficiency, high-temperature heat-exchangers. *Int J Hydrogen Energy* 32:3622–3630
- [83] Guan XM, Ye HQ (1980) Intergranular embrittlement caused by the precipitation of M_6C carbide containing silicon. *J Mater Sci* 15(2935):2937. <https://doi.org/10.1007/BF00550568>
- [84] Leitnaker JM, Klueh RL, Laing WR (1975) The composition of eta carbide phase in 2 1/4 Cr-1 Mo Steel. *Metall Trans A* 6:1949–1955
- [85] Maziasz PJ (1979) The precipitation response of 20%-cold worked type 316 stainless steel to simulated fusion irradiation. *J Nucl. Mater.* 85,86:713–717
- [86] Ecob RC, Lobb RC, Kohler VL (1987) The formation of G-phase in 20/25 Nb stainless steel AGR fuel cladding alloy and its effect on creep properties. *J Mater Sci.* 22(2867):2880. <https://doi.org/10.1007/BF01086484>
- [87] Evans N, Maziasz P, Truhan J (2005) Phase transformations during service aging of nickel based superalloy pyromet 31V. In: *Solid [to] solid phase transformations in organic materials*, pp 809–818
- [88] Ou M, Hao X, Ma Y, Liu R, Zhang L, Liu K (2018) Effect of carbon on the microstructure and stress rupture properties of a new Ni–Cr–W–Fe alloy for advanced ultra-supercritical power plants. *J Alloys Compd* 732:107–115
- [89] Sahlaoui H, Makhlof K, Sidhom H, Philibert J (2004) Effects of ageing conditions on the precipitates evolution, chromium depletion and intergranular corrosion susceptibility of AISI 316L: experimental and modeling results. *Mater Sci Eng A* 372:98–108
- [90] Shingledecker JP, Evans ND (2010) Creep-rupture performance of 0.07C-23Cr-45Ni-6W-Ti, Nb austenitic alloy (HR6W) tubes. *Int J Press Vessel Pip* 87:345–350
- [91] Gavriluk VG, Berns H (1999) *High nitrogen steels: structure, properties, manufacture, applications*, 1st edn. Springer, New York
- [92] Tu KN, Turnbull D (1967) Morphology of cellular precipitation of tin from lead-tin bicrystals. *Acta Metall* 15:369–376
- [93] Tu DTKN (1967) morphology of cellular precipitation of tin from lead-tin bicrystals-II. *Acta Metall* 15:1317–1323
- [94] Fournelle RA (1979) Discontinuous coarsening of lamellar cellular precipitate in an austenitic Fe-30 wt.%Ni-6 wt. % Ti alloy-II: growth kinetics. *Acta Metall* 27:1147–1155
- [95] Turnbull D (1955) Theory of cellular precipitation. *Acta Metall* 3:55–63
- [96] Aaronson HI, Liu YC (1968) On the Turnbull and the Cahn theories of the cellular reaction. *Scr Metall* 2:1–8
- [97] Shapiro JM, Kirkaldy JS (1968) The kinetics of discontinuous precipitation in copper-indium alloys. *Acta Metall* 16:1239–1252
- [98] Sundquist BE (1973) Cellular precipitation. *Metall Trans* 4:1919–1934

Publisher's Note Springer Nature remains neutral with regard to jurisdictional claims in published maps and institutional affiliations.